Article

Tuning Single-Atom Dopants on Manganese Oxide for Selective Electrocatalytic Cyclooctene Epoxidation

Minju Chung,[||] Kyoungsuk Jin,[||] Joy S. Zeng, Thu N. Ton, and Karthish Manthiram*

Read Online

ACCESS | Metrics & More | Article Recommendations | Supporting Information

ABSTRACT: Selective and efficient electrocatalysts are imperative for the successful deployment of electrochemistry toward synthetic applications. In this study, we used galvanic replacement reactions to synthesize iridium-decorated manganese oxide nanoparticles, which showed a cyclooctene epoxidation partial current density of 10.5 ± 2.8 mA/cm^2 and a Faradaic efficiency of $46 \pm 4\%$. Results from operando X-ray absorption spectroscopy suggest that manganese leaching from the nanoparticles during galvanic replacement introduces lattice vacancies that make the nanoparticles more susceptible to metal oxidation and catalyst reconstruction under an applied anodic potential. This results in an increased presence of electrophilic oxygen atoms on the catalyst surface during reaction conditions, which may contribute to the enhanced electrocatalytic activity toward cyclooctene epoxidation.
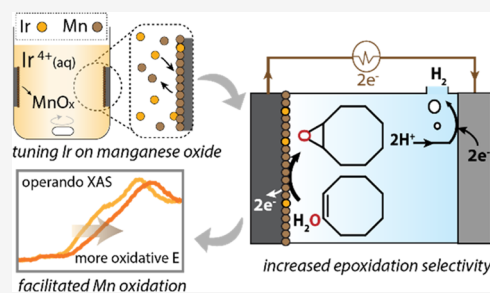
INTRODUCTION

The electrification of chemical reactions is an emerging strategy to reduce carbon emissions in the chemical industry. While thermodynamic analyses demonstrate that an electrical potential can efficiently drive various chemical reactions under mild conditions,[1] achieving high selectivity and activity toward a target reaction remains challenging. For the broader implementation of electricity-driven chemical synthesis, the discovery of high-performance electrocatalysts is critical.

Olefin epoxidation is a crucial chemical functionalization reaction that produces key chemical intermediates for the synthesis of various commercial end products.[2,3] For example, propylene oxide is produced via the chlorohydrin process, and ethylene oxide is chiefly synthesized using molecular oxygen and silver catalysts. In addition to these two processes, homogeneous catalysts containing terminal metal-oxo species have been reported as epoxidation catalysts.[4−6] Metal-oxo species generated by peroxide-based oxidants or photo-irradiation can provide oxygen atoms to olefin substrates to make epoxide or ketone products. Although these routes have exhibited a high selectivity and yield, there is a need to improve upon these efforts to circumvent elevated temperatures and pressures, undesirable stoichiometric byproducts, explosive peroxide-based oxidants,[7] and high catalyst separation costs. In this regard, a heterogeneous electrochemical process that can directly epoxidize olefins under ambient conditions presents an attractive alternative to the existing epoxidation routes.

Several research groups have recently attempted olefin epoxidation via electrochemical methods. In situ electrochemical generation of chemical oxidants such as hydrogen peroxide,[8−10] active halogens,[11,12] or peroxodicarbonate[13] were used to convert olefin substrates to their corresponding epoxides. Our group previously reported new electrochemical routes for olefin epoxidation, where sub-10-nm-sized manganese oxide nanoparticles catalyzed the direct epoxidation of cyclooctene using water as an oxygen atom source, with a faradaic efficiency of ∼30%.[14] Based on electrochemical kinetic studies, the generation of Mn(IV)=O species was suggested to be the resting state of the catalytic cycle, facilitating the transfer of the oxygen atom to the cyclooctene substrate. While this method provides an environmentally friendly and safe route to make epoxides, its low faradaic efficiency and yield must be improved for it to become industrially relevant.

One way to improve the efficiency of heterogeneous catalysts is through the introduction of atomically dispersed metal atoms on the appropriate supporting materials. These catalysts with atomically dispersed metal atoms have exhibited enhanced specific activity and high selectivity due to their unsaturated coordination environment, which facilitates their ability to act as active sites and achieve unexpected selectivity.[15−17] For catalysts where the isolated atoms act as the sole active site, arranging as many isolated atoms as possible on the substrate is desirable to maximize atom economy.[18] On the other hand, single metal centers can also be introduced to a substrate that already acts as a catalyst for the target reaction. In this case, it is important to consider the
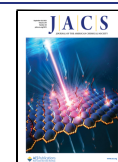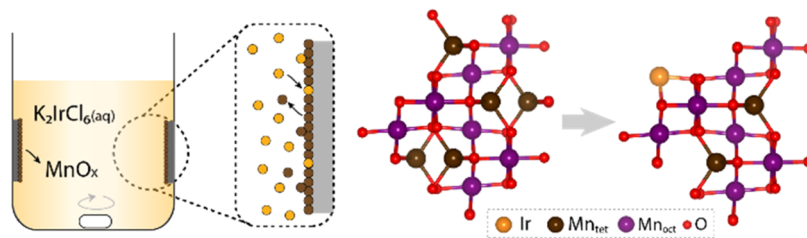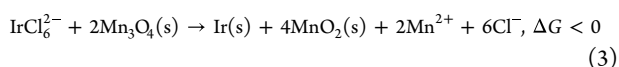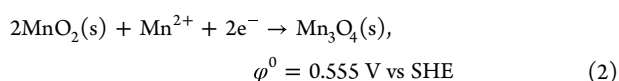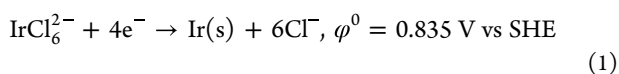
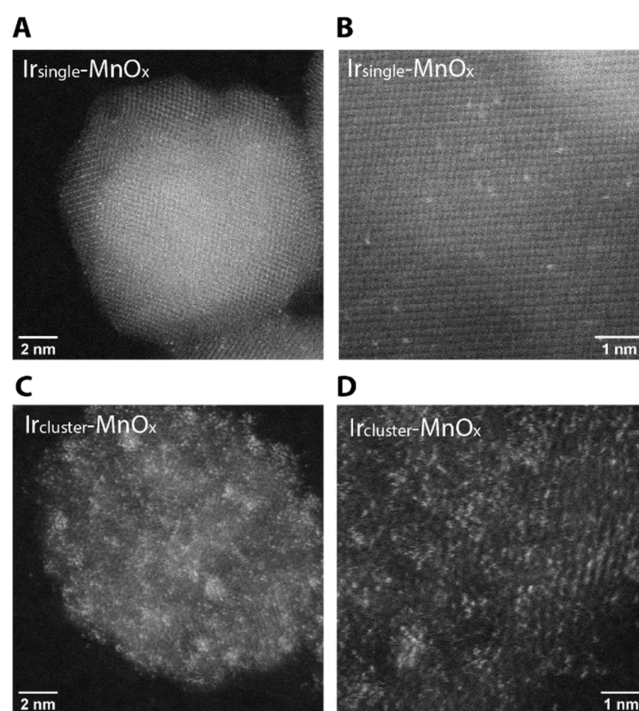**Figure 1.** Scheme of the galvanic replacement between the iridium precursor and manganese oxide catalyst.

geometric and electronic tuning of the original active sites upon the introduction of guest atoms to the host catalyst, in addition to their role as additional active sites. In this vein, we used a galvanic replacement method to attain single to cluster iridium atoms decorated on manganese oxide catalysts while generating manganese vacancies. This modification increases the selectivity of both manganese and iridium oxide catalysts toward olefin epoxidation. Herein, we report a new catalyst, single iridium-decorated manganese oxide nanoparticles (Ir_{single}-MnO_x NPs), which exhibited a nearly 50% faradaic efficiency for cyclooctene epoxidation. Furthermore, a series of electrochemical kinetic studies and operando X-ray absorption spectroscopy (XAS) analyses provided insights into the structure−activity relationship of cyclooctene epoxidation by Ir_{single}-MnO_x NPs.

RESULTS AND DISCUSSION

Synthesis of Ir-MnO_x NPs Using Galvanic Replacement Reaction. The MnO_x NPs of the Mn_3O_4 (hausmannite) phase were prepared via hot injection,[14] and iridium atoms were decorated on the surface of the nanoparticles by a galvanic replacement reaction (see the Experimental Section and Supporting Information for details). The galvanic reaction step involved a spontaneous redox reaction between K_2IrCl_6 and MnO_x nanoparticles deposited on a carbon paper substrate; simultaneous dissolution of manganese atoms and deposition of iridium heteroatoms on the surface are driven by the difference in the redox potential between the two metals involved.[19,20] Although the exact driving force varies depending on the local concentration of participating species and the details on the coordination environment on the surface, the standard electrode potential of the metals was used as a baseline for predicting the probability of a given pairing of metals toward galvanic replacement. The standard reduction potential of the iridium precursor (eq 1) is 0.835 V, while the reduction potential of the phase transition between β-MnO_2 and Mn_3O_4 was calculated to be 0.555 V (eq 2; see also Table S1).[21] The higher reduction potential of the iridium precursor allows for the spontaneous reduction of $IrCl_6^{2-}$ coupled with the oxidation of Mn_3O_4 (eq 3), which drives the deposition of iridium on the manganese oxide surface and the concomitant leaching of manganese (Figure 1).

$$IrCl_6^{2-} + 4e^- \rightarrow Ir(s) + 6Cl^-, \varphi^0 = 0.835 \text{ V vs SHE} \tag{1}$$

$$2MnO_2(s) + Mn^{2+} + 2e^- \rightarrow Mn_3O_4(s),$$
$$\varphi^0 = 0.555 \text{ V vs SHE} \tag{2}$$

$$IrCl_6^{2-} + 2Mn_3O_4(s) \rightarrow Ir(s) + 4MnO_2(s) + 2Mn^{2+} + 6Cl^-, \Delta G < 0 \tag{3}$$

Catalyst Characterizations. The Ir-MnO_x NPs were characterized using high-angle annular dark-field (HAADF) imaging with aberration-corrected scanning transmission electron microscopy (STEM). Incoherent Z-contrast imaging and high spatial resolution allowed the determination of the iridium atom distribution on the manganese oxide nanoparticle supports.[22] Under mild synthetic conditions, single iridium atoms were randomly dispersed in the MnO_x lattice, appearing as brighter spots in the STEM images (Ir_{single}-MnO_x; Figure 2A,B). The iridium loading was controlled by adjusting the

Figure 2. HAADF-STEM images of (A, B) Ir_{single}-MnO_x and (C, D) $Ir_{cluster}$-MnO_x.

concentration of the precursor and the temperature of the galvanic replacement reaction. Upon increasing the galvanic replacement reaction time, the concentration of the iridium precursor, and the reaction temperature, the loading of iridium atoms on the Ir-MnO_x surface also increased, leading to the formation of clusters (Figures S4 and 2C,D). The size and the number of clusters increased in the following order: Ir_{few}-MnO_x < $Ir_{few/cluster}$-MnO_x < $Ir_{cluster}$-MnO_x (see Section A.2. for details).
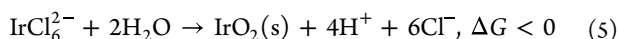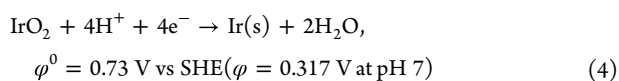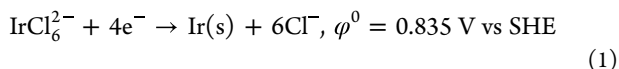
We then used XAS to probe the oxidation state and local coordination environment of the metals in the synthesized Ir-MnO_x, which encompasses samples ranging from single atoms (Ir_{single}-MnO_x) to clusters ($Ir_{cluster}$-MnO_x) (Figure 3). The
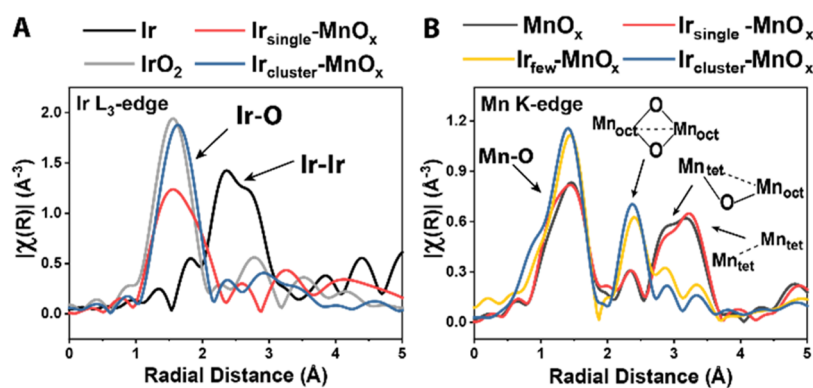
Figure 3. Fourier transform EXAFS spectra of Ir-MnO$_x$ samples at (A) the Ir L$_3$-edge and (B) the Mn K-edge. Note that the radial distance (scattering length) is ~0.5 Å shorter than the bond length between the scatterers.

extended X-ray absorption fine structure (EXAFS) at the Ir L$_3$-edge suggests that the short-range scattering features of Ir-MnO$_x$ resemble those of IrO$_2$, indicating that the iridium atoms are surrounded by oxygen for samples containing single atoms and clusters of iridium alike. The prominent peak at ~1.6 Å corresponds to the Ir−O scattering path, suggesting that iridium is coordinated by oxygen in Ir-MnO$_x$, which by itself might imply a local coordination environment similar to that of IrO$_2$. However, the second and higher shells of Ir-MnO$_x$ do not match IrO$_2$, which could indicate scattering paths from Ir−Mn instead of Ir−Ir. Furthermore, the lower intensity of the Ir−O peak in Ir$_{single}$-MnO$_x$ compared to IrO$_2$ or Ir$_{cluster}$-MnO$_x$ implies that iridium is undercoordinated in Ir$_{single}$-MnO$_x$. The estimated coordination number from the EXAFS fitting for iridium in Ir$_{single}$-MnO$_x$ was 5 ± 1, while Ir in IrO$_2$ has a coordination number of 6.

Compared to Ir$_{single}$-MnO$_x$, Ir$_{cluster}$-MnO$_x$ shares more similarities with IrO$_2$, which can be ascribed to another pair of galvanic reactions that oxidize iridium on the catalyst surface. For Ir$_{single}$-MnO$_x$, the ICP-OES analysis (Table S2) of the postgalvanic replacement solution showed that the amount of consumed iridium precursor was comparable to the amount of manganese leached out. However, for Ir$_{cluster}$-MnO$_x$, excess iridium was consumed from the solution relative to the amount of manganese that dissolved into the solution. The result suggests that the deposition of iridium beyond a certain point does not require manganese dissolution. Instead, the iridium deposition on the catalyst can be galvanically coupled with the oxidation of the iridium clusters, which are essentially combined as the hydrolysis of the iridium precursor on the MnO$_x$ surface (eq 5). It is worth noting that this favorable reaction does not imply that we should expect a well-defined crystalline IrO$_2$ phase on the surface. The reaction implies that the deposited iridium atoms have a tendency to be oxidized, forming bonds with neighboring oxygen atoms rather than remaining in a more reduced form.

$$IrCl_6^{2-} + 4e^- \rightarrow Ir(s) + 6Cl^-, \; \varphi^0 = 0.835 \text{ V vs SHE} \tag{1}$$

$$IrO_2 + 4H^+ + 4e^- \rightarrow Ir(s) + 2H_2O,$$
$$\varphi^0 = 0.73 \text{ V vs SHE}(\varphi = 0.317 \text{ V at pH 7}) \tag{4}$$

$$IrCl_6^{2-} + 2H_2O \rightarrow IrO_2(s) + 4H^+ + 6Cl^-, \; \Delta G < 0 \tag{5}$$

Manganese leaching during galvanic replacement generated lattice vacancies, which increased the average Mn oxidation

state in the nanoparticles (Figure S5). The average manganese oxidation states estimated from the X-ray absorption near-edge structure (XANES) followed the order: Mn$_3$O$_4$ < MnO$_x$ < Ir$_{single}$-MnO$_x$ < Ir$_{few}$-MnO$_x$ ≈ Ir$_{cluster}$-MnO$_x$ < MnO$_2$. A higher manganese oxidation state is correlated with a shortened Mn−O bond in Ir$_{few}$-MnO$_x$ and Ir$_{cluster}$-MnO$_x$ compared to that in MnO$_x$ and Ir$_{single}$-MnO$_x$, as shown by EXAFS at the Mn K-edge (Figure 3B). The EXAFS further revealed that pristine MnO$_x$ and Ir$_{single}$-MnO$_x$ both have Mn$_3$O$_4$-like structures, characterized by a Mn−Mn scattering path ($R_{Mn(oct)-Mn(tet)}$ = 3.495 Å) from corner-sharing octahedral Mn and tetrahedral Mn. In contrast, Ir$_{few}$-MnO$_x$ and Ir$_{cluster}$-MnO$_x$ exhibit MnO$_2$-like structures, showing a shorter Mn−Mn scattering path ($R_{Mn(oct)-Mn(oct)}$ = 2.93 Å) resulting from edge-sharing octahedral Mn atoms. This implied that the manganese oxidation state increased as the galvanic replacement reaction progressed, and the highly oxidized Ir-MnO$_x$ samples underwent reconstruction from a Mn$_3$O$_4$-like structure to a MnO$_2$-like structure.

The EXAFS fitting of the Mn K-edge was performed to probe the structural differences between MnO$_x$ and Ir$_{single}$-MnO$_x$. The first shells of the samples were fitted to the scattering path of Mn$_3$O$_4$. A linear combination fitting of the tetrahedral and octahedral Mn−O scattering paths on the first shells of MnO$_x$ and Ir$_{single}$-MnO$_x$ was performed to estimate the proportion of Mn at the tetrahedral site. The ratios of the Mn tetrahedral site in Ir$_{single}$-MnO$_x$ (0.2 ± 0.1) and MnO$_x$ (0.3 ± 0.1) are within the errors of each other (Table S3). For the Ir$_{few}$-MnO$_x$ and Ir$_{cluster}$-MnO$_x$ samples that were treated with a higher extent of galvanic replacement, Mn$_{tet}$−Mn$_{oct}$ and Mn$_{tet}$−Mn$_{tet}$ peaks in FT-EXAFS were diminished (Figure 3B). These results suggest that Mn(II) in tetrahedral sites may be liberated from the catalyst in exchange for iridium during galvanic deposition.

Electrochemical Kinetic Study. Ir$_{single}$-MnO$_x$ showed higher selectivity and activity for cyclooctene epoxidation than pristine MnO$_x$ (Figure 4A,B). Electrochemical kinetic studies were conducted by chronoamperometry at varying potentials and substrate concentrations. In a typical experiment, 10 C of charge was passed, which was equivalent to a maximum conversion of ~6.5% of the substrate. The partial current density toward epoxidation was higher with Ir$_{single}$-MnO$_x$ than with pristine MnO$_x$, showing an especially large gap at potentials above 1.3 V vs Fc/Fc$^+$. Compared with MnO$_x$, the epoxidation rate increased more rapidly with Ir$_{single}$-MnO$_x$ in response to the applied potential. Rate law analysis
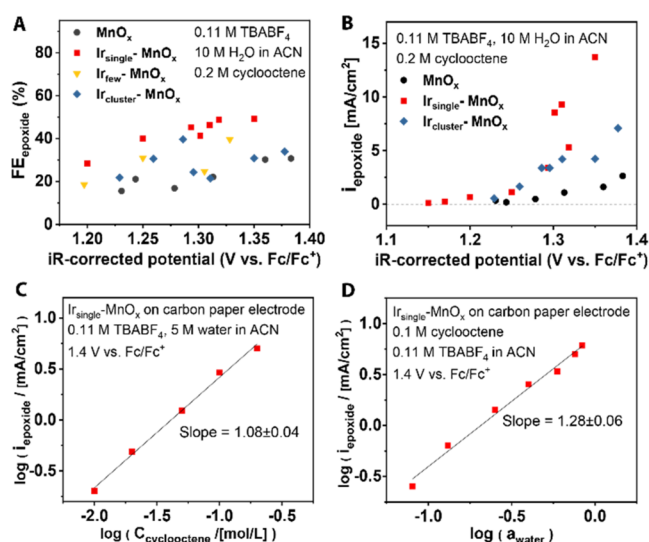
Figure 4. Ir-MnO$_x$ catalysts for cyclooctene epoxidation. (A) Faradaic efficiency for cyclooctene epoxidation vs potentials. (B) Comparison of average epoxidation current between Ir$_{single}$-MnO$_x$, Ir$_{cluster}$-MnO$_x$, and MnO$_x$. (C) Cyclooctene concentration (at 5 M H$_2$O) and (D) water concentration (at 100 mM cyclooctene) dependences of average epoxide partial current at 1.4 V vs Fc/Fc$^+$. Acetonitrile (ACN) was used as the solvent.

conducted using Ir$_{single}$-MnO$_x$ NPs showed a first-order dependence on the cyclooctene concentration and water activity (Figure 4C,D). These results are consistent with the mechanism proposed for the epoxidation of olefins by Mn$_3$O$_4$-based NP catalysts (see Figure S6 and relevant discussion in Supporting Information Section E).[14] In our previous work, we proposed Mn(IV)=O as the reactive intermediate that transfers the oxygen atom to the olefin substrate, leaving Mn(II)-vacant sites. Considering the nucleophilic nature of the carbon–carbon double bond in cyclooctene, increasing the electrophilicity of the oxygen atom on the catalyst may facilitate epoxidation.[23,24] As discussed earlier, XAS analysis showed that the average oxidation state of manganese in MnO$_x$ increased after iridium decoration and the introduction of manganese vacancies via galvanic replacement. The increase in the formal oxidation state of manganese might increase the electrophilic character on the oxygen ligands by the induced hole-doping effect.[25] This might explain why Ir$_{single}$-MnO$_x$ showed more selective epoxidation capability than pristine MnO$_x$.

However, Ir-MnO$_x$ with higher iridium loadings was not as selective as Ir$_{single}$-MnO$_x$ for cyclooctene epoxidation. Notably, Ir$_{single}$-MnO$_x$ exhibited a distinct structure from Ir$_{few}$- or Ir$_{cluster}$-MnO$_x$. Ir$_{single}$-MnO$_x$ can be described as a Mn$_3$O$_4$-like structure decorated with unclustered iridium atoms on its surface. In contrast, Ir$_{few}$- and Ir$_{cluster}$-MnO$_x$ contained aggregated iridium atoms on their surfaces. Clusters of oxidized iridium on the surface can provide active sites that are more selective toward oxygen evolution than epoxidation since iridium oxides are well-established water oxidation catalysts.[26] Iridium oxide nanoparticles exhibited lower epoxidation selectivity than MnO$_x$ or Ir-MnO$_x$ catalysts with an FE$_{epoxide}$ = 25 ± 3% (n = 2) at 1.45 V vs Fc/Fc$^+$ (85% iR-compensated) using 0.2 M cyclooctene and 10 M H$_2$O.

We have investigated other heteroatom-decorated metal oxide nanocatalysts to find out if there are better combinations

for epoxidation. The galvanic replacement was also performed using other heteroatoms and supporting metal oxide catalysts. Pt$_{single}$-MnO$_x$ was synthesized with K$_2$PtCl$_6$ instead of K$_2$IrCl$_6$ (Figure S7A), but the FE$_{epoxide}$ did not increase significantly (from 25 to 30% for MnO$_x$ to 33% for Pt$_{single}$-MnO$_x$). When FeO$_x$ was used instead of MnO$_x$, atomic iridium was successfully dispersed on FeO$_x$ (Figure S7B), but the modification did not result in any improvement in the epoxidation selectivity (FE$_{epoxide}$ = 12%) or activity (Table S6). A specific combination of iridium and MnO$_x$ was required to achieve enhanced epoxidation selectivity upon decorating the base metal oxide with single atoms.

Operando XAS at Mn K-Edge and Ir L$_3$-Edge. To directly probe the relationship between the catalyst properties and performance, operando XAS at the Mn K-edge and Ir L$_3$-edge was conducted. The manganese oxidation state under anodic bias increased more dramatically after single iridium atoms were deposited on the surface of MnO$_x$ (Figure 5A,B).
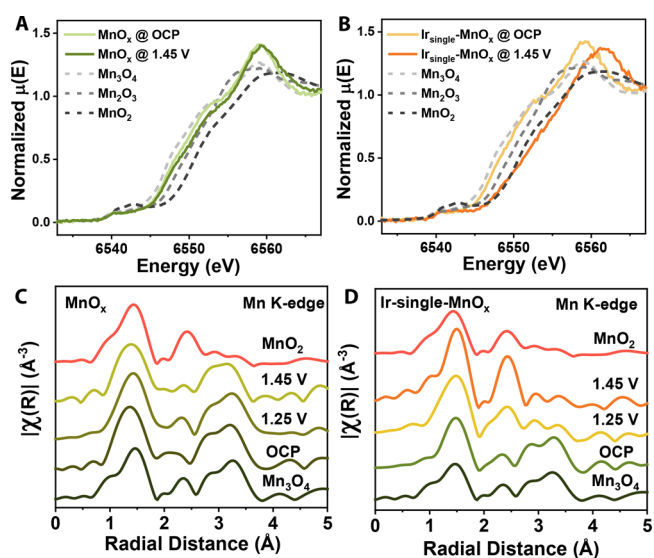
Figure 5. Operando XAS at the Mn K-edge. Shifts in XANES spectra for (A) MnO$_x$ and (B) Ir$_{single}$-MnO$_x$ catalysts. Fourier transform EXAFS spectra for (C) MnO$_x$ and (D) Ir$_{single}$-MnO$_x$ catalysts. The potentials are 85% iR-compensated.

This result implies facile oxidation of manganese when MnO$_x$ is decorated with iridium to form Ir$_{single}$-MnO$_x$, generating the electrophilic oxygen species that participate in epoxidation. Moreover, we tracked the manganese coordination environment in MnO$_x$ and Ir$_{single}$-MnO$_x$ under epoxidation conditions with increasing anodic potential (Figure 5C,D). Although MnO$_x$ remained in its Mn$_3$O$_4$-like structure throughout the entire experiment, Ir-MnO$_x$ transformed from a Mn$_3$O$_4$-like structure into a MnO$_2$-like structure as the applied anodic potential increased. In Mn$_3$O$_4$, tetrahedral Mn(III) oxidized from Mn(II) is kinetically trapped to remain as Mn(III), and the oxidation of octahedral Mn(III) is sluggish due to stabilization by Jahn–Teller distortion.[27] This explains why MnO$_x$ retains its structure and initial oxidation state under increasing anodic potential. Meanwhile, mild tuning of MnO$_x$ with iridium single atoms facilitates manganese oxidation and the associated phase change under anodic potentials.

Structural information also provides insight into the higher performance of Ir$_{single}$-MnO$_x$ compared to Ir$_{few}$-MnO$_x$ and Ir$_{cluster}$-MnO$_x$. We characterized the catalysts with X-ray

photoelectron spectroscopy (XPS) to collect surface-specific information. While a higher extent of galvanic replacement could increase the initial oxidation state of manganese and the electrophilicity of the lattice oxygen atoms, there is a good chance that the metal-depleted oxygen atoms can take up protons, forming hydroxyl groups on the surface. In the case of iridium-decorated MnO_x NPs, we observed a peak at ~531.5 eV in the O 1s XPS spectrum, corresponding to characteristic surface hydroxyl groups (−OH) (Figure S8). Interestingly, predominant hydroxyl peaks were observed at the spectra of $Ir_{cluster}$-MnO_x compared to those of Ir_{single}-MnO_x or MnO_x nanoparticles. Similarly, Pt-MnO_x also exhibited a similar fashion in the O 1s XPS spectrum. Pt_{single}-MnO_x showed a higher abundance of hydroxyl species (Figure S9A), and the manganese oxidation state of Pt_{single}-MnO_x was higher than that of Ir_{single}-MnO_x (Figure S9B). High coverage of surface hydroxyl species has been suggested as a descriptor for an enhanced oxygen evolution reaction (OER) activity.[28] Considering that the OER is a major competing reaction of cyclooctene epoxidation (Figure S11) and electrophilic oxygen species were believed to be responsible for a higher OER activity,[25] we believe that the $Ir_{cluster}$-MnO_x and Pt-MnO_x catalysts showed low selectivity toward epoxidation due to the surface hydroxyl species. Therefore, we would like to emphasize that achieving an appropriate degree of manganese oxidation and oxygen electrophilicity, in addition to the lack of iridium clusters on the surface, is important to suppress the OER while achieving an enhanced epoxidation activity.

The oxidation states of iridium in the Ir-MnO_x catalysts can be inferred from the Ir L_3-edge XANES spectrum, which is characterized by broad white lines corresponding to a transition from occupied 2p to empty 5d states. The higher white line indicates less-occupied d-orbital states and, thus, a lower electron density.[29] Moreover, the shift of the white line position is proportional to the oxidation state of iridium species in iridium oxides. The white line positions of Ir-MnO_x samples are at lower energy compared to that of IrO_2, indicating that its iridium oxidation state before applying the potential is lower than +4 (Figure 6A). The lower oxidation state of iridium in Ir_{single}-MnO_x is consistent with its longer Ir−O bond lengths compared to that in IrO_2. The estimated Ir−O bond length from EXAFS fitting was longer for lower Ir loading samples: 1.983 ± 0.006 Å (IrO_2) < 2.04 ± 0.01 Å ($Ir_{cluster}$-MnO_x) < 2.08 ± 0.02 Å (Ir_{single}-MnO_x).

Upon applying an anodic potential, the edge shift and white line increase were not apparent in the IrO_2 nanoparticle (~12 nm) catalysts (Figure 6B), presumably due to its small surface-to-bulk ratio. In contrast, the white line positions in Ir-MnO_x samples clearly shifted to higher energy (Figure 6C,D), which indicates that the iridium atoms as well as manganese atoms contributed to making the adjacent oxygen atom more electrophilic by creating electron-poor metal sites.

CONCLUSIONS

We probed the electronic states and local geometric structures of the Ir_{single}-MnO_x catalyst under electrochemical cyclooctene epoxidation conditions using operando XAS. The mild galvanic replacement tuning of MnO_x with iridium single atoms enabled dynamic catalyst reconstruction and facile metal oxidation under an anodic potential. Highly electrophilic oxygen atoms induced by adjacent electron-poor metals were possibly responsible for the enhanced electrocatalytic cyclooctene epoxidation performance on Ir_{single}-MnO_x compared to
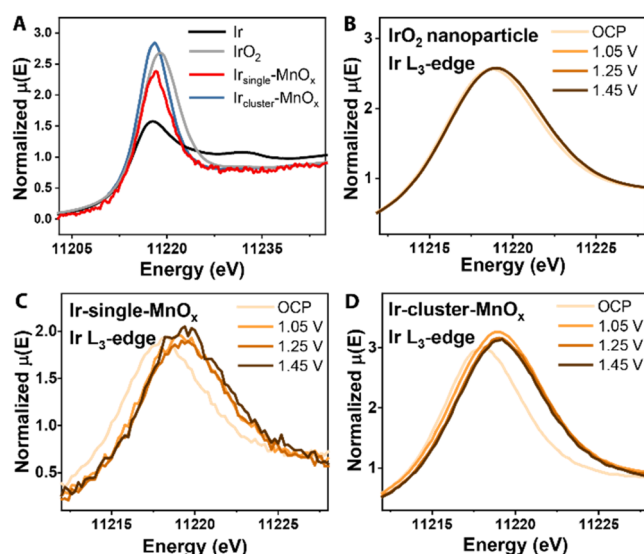
Figure 6. XANES at the Ir L_3-edge. (A) Comparison of the Ir L_3-edge white line for iridium reference materials and Ir-MnO_x catalysts. Edge shifts were examined for (B) IrO_2 nanoparticles, (C) Ir_{single}-MnO_x, and (D) $Ir_{cluster}$-MnO_x under applied anodic potential. The potentials are 85% iR-compensated.

undecorated MnO_x. The lower selectivity toward epoxidation with pre-reconstructed Ir_{few}-MnO_x and $Ir_{cluster}$-MnO_x catalysts can be attributed to the prevalent surface hydroxyl species and oxidized iridium clusters on the catalyst. Our findings highlight that galvanic replacement reactions can be used for the mild tuning of metal oxide catalysts by introducing heteroatoms as well as by modifying the structural and electronic properties of the catalyst.

■ EXPERIMENTAL SECTION

Electrode Preparation. Sub-10-nm-sized manganese oxide nanoparticles (MnO_x NPs) were synthesized by hot-injection and deposited on hydrophilic carbon paper (CP) electrodes. A series of Ir-MnO_x NPs were prepared from the deposited MnO_x NPs via the galvanic replacement method. Four MnO_x/CP electrodes were added to the beaker using a Kapton tape. The beaker was filled with an aqueous solution of K_2IrCl_6 and placed in a water bath. The temperature, reaction time, and precursor concentration were adjusted to tune the iridium loading on the MnO_x NPs (see the detailed synthesis procedure in the Supporting Information). The prepared electrodes were used as anodes for electrochemical studies.

Electrochemical Study. A sandwich-type one-compartment cell was used for the electrochemical studies. Platinum foil and Ag/AgCl electrodes acted as the cathode and reference electrodes, respectively. Acetonitrile (ACN) with 0.11 M tetrabutylammonium tetrafluoroborate ($TBABF_4$) was used as the electrolyte, with varying concentrations of cis-cyclooctene and water. Potentials were either 100% iR-compensated (i = current, R = resistance) manually or 85% iR-compensated automatically based on the initial electrochemical impedance spectroscopy results. After electrolysis, additional water, excess hexane, and an internal standard, 1,3,5-trimethoxybenzene, were added to the electrolyte. Oxidation products dissolved in the electrolyte were extracted into the hexane layer and quantified using nuclear magnetic resonance (NMR) spectroscopy. The gas-phase products, including hydrogen and oxygen, were quantified using on-line gas chromatography (SRI Instruments), with N_2 gas flowing through the cell as a carrier gas.

X-ray Absorption Spectroscopy. Operando XAS spectra were collected in X-ray fluorescence mode at beamlines 8-ID (Ir L_3-edge) and 7-BM (Mn K-edge) of the National Synchrotron Light Source II and 10.3.2 (Mn K-edge) of the Advanced Light Source. The same set

of electrochemical cells used for the kinetic studies was used, except for a backplate with a hole for the X-ray entrance. A Kapton polyimide film was placed between the window and electrode to prevent electrolyte leakage (Figure S12). All XAS data were processed using the Athena software for background removal and normalization. The EXAFS data were further modeled and analyzed using the Artemis software. The amplitude reduction factor (S_0^2) for each metal edge was determined by fitting the reference material with known coordination numbers. The S_0^2 values were used in other simulations to estimate the coordination numbers of the samples.

ASSOCIATED CONTENT

ⓈⒾ Supporting Information

The Supporting Information is available free of charge at https://pubs.acs.org/doi/10.1021/jacs.2c04711.

> Experimental methods including materials, catalyst, and electrode preparation; TEM analysis; electrochemical methods; product analysis; additional data; and discussions on the mechanism (PDF)

AUTHOR INFORMATION

Corresponding Author

Karthish Manthiram − *Division of Chemistry and Chemical Engineering, California Institute of Technology, Pasadena, California 91125, United States;* ⓞ orcid.org/0000-0001-9260-3391; Email: karthish@caltech.edu

Authors

Minju Chung − *Department of Chemical Engineering, Massachusetts Institute of Technology, Cambridge, Massachusetts 02139, United States;* ⓞ orcid.org/0000-0003-4359-7508

Kyoungsuk Jin − *Department of Chemical Engineering, Massachusetts Institute of Technology, Cambridge, Massachusetts 02139, United States; Department of Chemistry, Korea University, Seoul 02841, Republic of Korea;* ⓞ orcid.org/0000-0003-3009-6691

Joy S. Zeng − *Department of Chemical Engineering, Massachusetts Institute of Technology, Cambridge, Massachusetts 02139, United States;* ⓞ orcid.org/0000-0002-3443-3504

Thu N. Ton − *Division of Chemistry and Chemical Engineering, California Institute of Technology, Pasadena, California 91125, United States;* ⓞ orcid.org/0000-0003-0134-2435

Complete contact information is available at:
https://pubs.acs.org/10.1021/jacs.2c04711

Author Contributions

‖M.C. and K.J. contributed equally to this work. All authors have given approval to the final version of the manuscript.

Notes

The authors declare no competing financial interest.

ACKNOWLEDGMENTS

REFERENCES

(1) Schiffer, Z. J.; Limaye, A. M.; Manthiram, K. Thermodynamic Discrimination between Energy Sources for Chemical Reactions. *Joule* **2021**, *5*, 135−148.

(2) Lane, B. S.; Burgess, K. Metal-Catalyzed Epoxidations of Alkenes with Hydrogen Peroxide. *Chem. Rev.* **2003**, *103*, 2457−2474.

(3) McGarrigle, E. M.; Gilheany, D. G. Chromium− and Manganese−salen Promoted Epoxidation of Alkenes. *Chem. Rev.* **2005**, *105*, 1563−1602.

(4) Lee, Y.-M.; Fukuzumi, S.; Nam, W.; Shen, D.; Saracini, C.; Sun, W. Photocatalytic Asymmetric Epoxidation of Terminal Olefins Using Water as an Oxygen Source in the Presence of a Mononuclear Non-Heme Chiral Manganese Complex. *J. Am. Chem. Soc.* **2016**, *138*, 15857−15860.

(5) Wang, B.; Lee, Y. M.; Tcho, W. Y.; Tussupbayev, S.; Kim, S. T.; Kim, Y.; Seo, M. S.; Cho, K.; Dede, Y.; Keegan, B. C.; Ogura, T.; Kim, S. H.; Ohta, T.; Baik, M. H.; Ray, K.; Shearer, J.; Nam, W. Synthesis and Reactivity of a Mononuclear Non-Haem Cobalt(IV)-Oxo Complex. *Nat. Commun.* **2017**, *8*, No. 14839.

(6) Lee, Y. M.; Yoo, M.; Yoon, H.; Li, X. X.; Nam, W.; Fukuzumi, S. Direct Oxygen Atom Transfer versus Electron Transfer Mechanisms in the Phosphine Oxidation by Nonheme Mn(IV)-Oxo Complexes. *Chem. Commun.* **2017**, *53*, 9352−9355.

(7) Lane, B. S.; Burgess, K. A Cheap, Catalytic, Scalable, and Environmentally Benign Method for Alkene Epoxidations. *J. Am. Chem. Soc.* **2001**, *123*, 2933−2934.

(8) Espinal, L.; Suib, S. L.; Rusling, J. F. Electrochemical Catalysis of Styrene Epoxidation with Films of MnO 2 Nanoparticles and H2O2. *J. Am. Chem. Soc.* **2004**, *126*, 7676−7682.

(9) Nishihara, H.; Pressprich, K.; Murray, R. W.; Coliman, J. P. Electrochemical Olefin Epoxidation with Manganese Meso-Tetraphenylporphyrin Catalyst and Hydrogen Peroxide Generation at Polymer-Coated Electrodes. *Inorg. Chem.* **1990**, *29*, 1000−1006.

(10) Ho, K.-P.; Wong, K.-Y.; Chan, T. H. Indirect Catalytic Epoxidation with Hydrogen Peroxide Electrogenerated in Ionic Liquids. *Tetrahedron* **2006**, *62*, 6650−6658.

(11) Chung, M.; Jin, K.; Zeng, J. S.; Manthiram, K. Mechanism of Chlorine-Mediated Electrochemical Ethylene Oxidation in Saline Water. *ACS Catal.* **2020**, *10*, 14015−14023.

(12) Leow, W. R.; Lum, Y.; Ozden, A.; Wang, Y.; Nam, D.-H.; Chen, B.; Wicks, J.; Zhuang, T.-T.; Li, F.; Sinton, D.; Sargent, E. H. Chloride-Mediated Selective Electrosynthesis of Ethylene and Propylene Oxides at High Current Density. *Science* **2020**, *368*, 1228−1233.

(13) Seitz, A.; Kohlpaintner, P. J.; van Lingen, T.; Dyga, M.; Sprang, F.; Zirbes, M.; Waldvogel, S. R.; Gooßen, L. J. Concentrated Aqueous Peroxodicarbonate: Efficient Electrosyn- Thesis and Use as Oxidizer in Epoxidations, S-, and N -Oxidations. *Angew. Chem., Int. Ed.* **2022**, *61*, No. e202117563.

(14) Jin, K.; Maalouf, J. H.; Lazouski, N.; Corbin, N.; Yang, D.; Manthiram, K. Epoxidation of Cyclooctene Using Water as the Oxygen Atom Source at Manganese Oxide Electrocatalysts. *J. Am. Chem. Soc.* **2019**, *141*, 6413−6418.

(15) Yang, X. F.; Wang, A.; Qiao, B.; Li, J.; Liu, J.; Zhang, T. Single-Atom Catalysts: A New Frontier in Heterogeneous Catalysis. *Acc. Chem. Res.* **2013**, *46*, 1740−1748.

(16) Zhang, H.; Liu, G.; Shi, L.; Ye, J. Single-Atom Catalysts: Emerging Multifunctional Materials in Heterogeneous Catalysis. *Adv. Energy Mater.* **2018**, *8*, No. 1701343.

(17) Wang, A.; Li, J.; Zhang, T. Heterogeneous Single-Atom Catalysis. *Nat. Rev. Chem.* **2018**, *2*, 65−81.

(18) Wang, Q.; Huang, X.; Zhao, Z. L.; Wang, M.; Xiang, B.; Li, J.; Feng, Z.; Xu, H.; Gu, M. Ultrahigh-Loading of Ir Single Atoms on NiO Matrix to Dramatically Enhance Oxygen Evolution Reaction. *J. Am. Chem. Soc.* **2020**, *142*, 7425−7433.

(19) Kim, K. W.; Kim, S. M.; Choi, S.; Kim, J.; Lee, I. S. Electroless Pt Deposition on Mn 3O 4 Nanoparticles via the Galvanic Replacement Process: Electrocatalytic Nanocomposite with Enhanced Performance for Oxygen Reduction Reaction. *ACS Nano* **2012**, *6*, 5122−5129.

(20) Nam, K.-T.; Jin, K.-S.; Jeong, D.-H.; Jerng, S.-E. Oxygen-Generating Catalyst, Electrode and Electrochemical Reaction System. European Patent EP3211125B1, 2020.

(21) Bratsch, S. G. Standard Electrode Potentials and Temperature Coefficients in Water at 298.15 K. *J. Phys. Chem. Ref. Data* **1989**, *18*, 1.

(22) Pennycook, S. J.; Jesson, D. E.; Mcgibbon, A. J. Incoherent Imaging by Z-Contrast Stem: Towards 1Å Resolution. *MRS Proc.* **1994**, *332*, 607.

(23) van der Eijk, J. M.; Peters, T. J.; de Wit, N.; Colijn, H. A. Electrochemical Epoxidation of Olefins. *Catal. Today* **1988**, *3*, 259−266.

(24) Linic, S.; Barteau, M. A. Construction of a Reaction Coordinate and a Microkinetic Model for Ethylene Epoxidation on Silver from DFT Calculations and Surface Science Experiments. *J. Catal.* **2003**, *214*, 200−212.

(25) Nong, H. N.; Reier, T.; Oh, H. S.; Gliech, M.; Paciok, P.; Vu, T. H. T.; Teschner, D.; Heggen, M.; Petkov, V.; Schlögl, R.; Jones, T.; Strasser, P. A Unique Oxygen Ligand Environment Facilitates Water Oxidation in Hole-Doped IrNiOx Core−Shell Electrocatalysts. *Nat. Catal.* **2018**, *1*, 841−851.

(26) Hidalgo-Acosta, J. C.; Méndez, M. A.; Scanlon, M. D.; Vrubel, H.; Amstutz, V.; Adamiak, W.; Opallo, M.; Girault, H. H. Catalysis of Water Oxidation in Acetonitrile by Iridium Oxide Nanoparticles. *Chem. Sci.* **2015**, *6*, 1761−1769.

(27) Chan, Z. M.; Kitchaev, D. A.; Weker, J. N.; Schnedermann, C.; Lim, K.; Ceder, G.; Tumas, W.; Toney, M. F.; Nocera, D. G. Electrochemical Trapping of Metastable Mn^{3+} Ions for Activation of MnO$_2$ Oxygen Evolution Catalysts. *Proc. Natl. Acad. Sci. U.S.A.* **2018**, *115*, E5261−E5268.

(28) Reier, T.; Pawolek, Z.; Cherevko, S.; Bruns, M.; Jones, T.; Teschner, D.; Selve, S.; Bergmann, A.; Nong, H. N.; Schlögl, R.; Mayrhofer, K. J. J.; Strasser, P. Molecular Insight in Structure and Activity of Highly Efficient, Low-Ir Ir-Ni Oxide Catalysts for Electrochemical Water Splitting (OER). *J. Am. Chem. Soc.* **2015**, *137*, 13031−13040.

(29) Monteseguro, V.; Sans, J. A.; Cuartero, V.; Cova, F.; Abrikosov, I. A.; Olovsson, W.; Popescu, C.; Pascarelli, S.; Garbarino, G.; Jönsson, H. J. M.; Irifune, T.; Errandonea, D. Phase Stability and Electronic Structure of Iridium Metal at the Megabar Range. *Sci. Rep.* **2019**, *9*, No. 8940.